Analysis of GeSn-SiGeSn Hetero-Tunnel FETs

Saurabh Sant*, Qing-Tai Zhao†, Dan Buca†, Siegfried Mantl†, and Andreas Schenk*
*Integrated Systems Laboratory, ETH Zurich, CH-8092 Zürich, Switzerland
†Peter-Grünberg-Institute, Forschungszentrum Jülich, 52425 Jülich, Germany

Email: sasant@iis.ee.ethz.ch

I. Introduction

Among the alloys of Group IV semiconductors the Germanium-Tin (GeSn) alloy is particularly interesting as it exhibits a small and direct band gap for a certain range of Sn content [1]. This feature can be exploited for high-performance tunnel FET (TFET) application [2], [3]. The small direct band gap enhances the band-to-band-tunneling (BTBT) rate which results in a high on-current. In order to reduce the off-state leakage, Silicon-Germanium-Tin (SiGeSn) alloys can be used in the drain region of the TFET. Addition of Si to GeSn increases the band gap of the alloy, thus reducing the ambipolar behavior. Therefore, the GeSn/SiGeSn heterostructure system is a promising candidate for TFET application. In this work, the performance of GeSn/SiGeSn TFETs is studied by combining the empirical pseudopotential method (EPM) with 2D/3D technology-computer-aided-design (TCAD) simulations of realistic geometries.

II. Pseudopotential Calculations of GeSn-SiGeSn Alloy System

TCAD modeling of realistic hetero TFETs requires the band structure quantities such as band offsets, direct and indirect band gaps, and effective masses for the given semiconductors. In this work, the nonlocal EPM is used to obtain these band structure parameters for different alloy compositions. Pseudopotential parameters of Sn are extracted with S-Band [4] by fitting the calculated band energies to experimental data. The fitting exercise provides a reasonable match between measured and calculated band energies. The parameters of Si and Ge are taken from Ref. [5]. These parameters are listed in Table I. The Virtual Crystal Approximation (VCA) is employed to model the band structure of GeSn and SiGeSn alloys. The variation of lattice constants of GeSn and SiGe with the alloy composition is modeled using quadratic expressions fitted to the experimental lattice constants [6].

TABLE I: EPM parameter values for Si, Ge and Sn. The parameter values of Si and Ge are taken from Ref. [5]

Parameter	Unit	Si	Ge	Sn
$V_{loc}(\sqrt{3})$	Ry	-0.2307	-0.2378	-0.21
$V_{loc}(\sqrt{8})$	Ry	0.0518	0.02852	0.02359
$V_{loc}(\sqrt{11})$	Ry	0.06878	0.0469	0.01737
α_0	Ry	0.02815	0.0	0.0
β_0	1	0.0	0.0	0.365
R_0	Å	1.0599	0.0	1.0
α_2	Ry	0.0	0.309	0.71
R_2	Å	0.0	1.2788	1.453
μ	Ry	0.00018	0.000965	0.00239
ζ	1	0.53	0.45	3.97
q^2 cutoff	$(\frac{2\pi}{a_0})^2$	11.5	12.44	15.25
`nonLocalWell`		Square	Square	Square

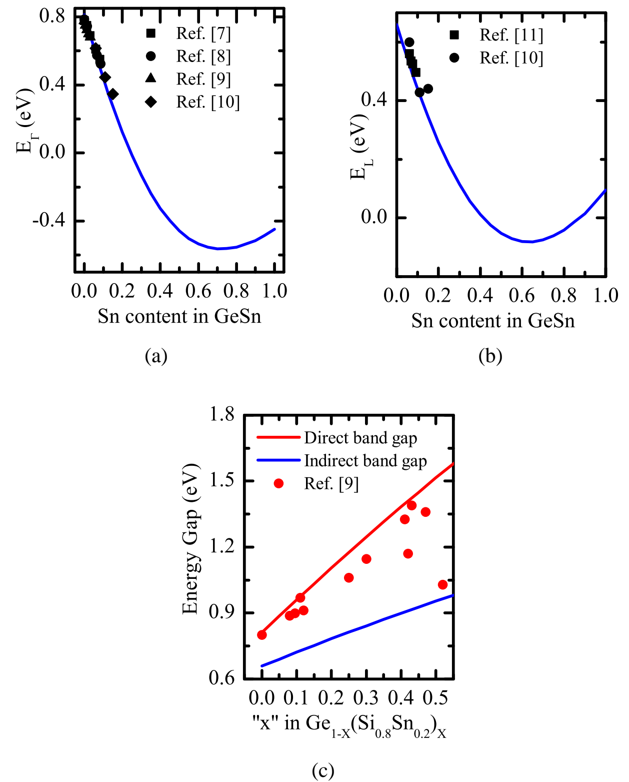

Fig. 1: Comparison of experimental and calculated values of (a) direct band gap in GeSn, (b) indirect band gap in GeSn and (c) direct and indirect band gaps in SiGeSn.

A comparison of the band energies calculated using EPM with the experimentally extracted band energies is shown in Fig. 1. Both direct and indirect band gaps in GeSn show good agreement with the experiments. The EPM calculations predict a crossover of the GeSn alloy from an indirect band gap material to a direct band gap material at a Sn content of about 10%. The calculations also suggest that the alloy will exhibit a negative band gap for Sn mole fractions higher than 25%. A comparison between calculated and experimental band gaps in SiGeSn is given in Fig. 1(c). The experimental data have been extracted from photoluminescence measurements [12]. The data show a large deviation from the calculated band energies at intermediate x. This could be explained as follows. For small x, the difference between direct and indirect gaps is small, giving a dominant peak corresponding to the direct gap. At intermediate x, this difference is significant which results in a dominant peak due to indirect transitions. It is interesting

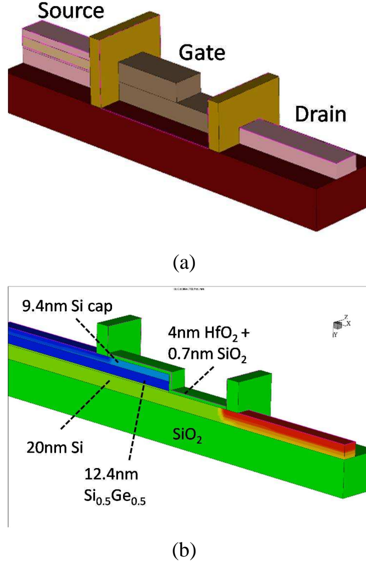

(a)

(b)

Fig. 2: (a) Device structure of $Si_{0.5}Ge_{0.5}$/Si heterojunction nanowire-TFET simulated using 3D simulations. (b) A vertical cut along the plane of symmetry. It shows the doping profiles and the structure of the TFET.

to note that a good reproduction of the experimental data is achieved *without* employing bowing of the EPM parameters. Having achieved reasonable agreement with the experiments, the pseudopotential calculations were used to determine the band structure quantities required to model BTBT in device simulations with S-Device [13].

III. Simulation of heterostructure Tunnel FETs

First, 3D simulations of $Si_{0.5}Ge_{0.5}$/Si heterostructure TFETs [14] were performed by taking the EPM band structure quantities as inputs for the BTBT model. These parameters are listed in Table II. The TFET has the form of a lateral nanowire etched from Si-cap/p++ - $Si_{0.5}Ge_{0.5}$/n-Si heterostructures grown over SiO_2. Etching the nanowires down to Si at one end results in a step-like structure as shown in Fig. 2(a). The gate consists of a 4 nm thick HfO_2 layer in addition to a ~ 7 Å thick native oxide (total EOT = ~ 1.4 nm). The gate covers the step as revealed by the cut-plane (Fig. 2(b)). The "nonlocal dynamic path BTBT model" and Shockley-Read-Hall (SRH) generation-recombination model were employed in the simulations. The major contribution to the BTBT current comes from under-the-gate tunneling ("line tunneling") in the SiGe layer along the vertical side-walls which necessitates 3D simulations. The simulated I_D-V_G characteristics of the device match well with the experimental I_D-V_G curves (Fig. 3(a)) after adjusting the gate work function (i.e. increasing it from 4.25 eV to 5.1 eV). The slight underestimation of I_D at low V_G in the simulation is attributed to trap-assisted tunneling due to the defects present both at the SiGe/Si as well as the HfO_2/SiGe interface (not modeled). The simulated I_D-V_D curves (Fig. 3(b)) show qualitative resemblance, although the current values differ significantly. This difference may come from charge quantization in the channel region which is not modeled here. The SiGe layer was assumed to be fully relaxed when calculating BTBT parameters. Presence of strain in the layer doesn't change the subthreshold characteristics but could reduce the on-state current as can be seen in Fig. 3(c).

Device simulations were performed to select the optimum alloy compositions in the GeSn/SiGeSn system. Only the lattice-matched alloy compositions were considered to avoid strain relaxation-induced defects at the hetero interface. To incorporate this constraint, the Sn mole fraction in SiGeSn was fixed depending on the Si content in SiGeSn (henceforth referred to as "x") and the Sn content in GeSn (henceforth referred to as "y"). Thus, the design space changes from a three-dimensional space to a two-dimensional space. The simulations were performed for a range of suitable x and y and for a range of doping concentrations in the GeSn layer. Direct and phonon-assisted BTBT was modeled by the Kane model [15], [16], carrier redistribution due to quantization near the gate-source interface by the semiclassical MLDA model [17]. A double-gate TFET device geometry was selected for the simulations (Fig. 4(a)). The gate voltage at which the BTBT current starts to dominate the SRH generation current is defined as V_{off} and the corresponding current is defined as I_{off}. The subthreshold swing is averaged over four decades of I_D above I_{off} and the on-current is probed at $V_{on} = V_{off} + 0.5$ V (see Fig. 4(b)). The on-current density is calculated by dividing the on-current per μm by two times the length of the gate-source overlap. The SS and the on-current density are plotted as a function of source doping for a Sn mole fraction of 6% in the source (Fig. 4(c)). The plot in Fig. 4(c) suggests a reduction of the on-current after a certain optimum doping concentration as result of carrier redistribution due to quantization. From the plot, the source doping of 1e19 cm^{-3} - 4e19 cm^{-3} seems to be the optimal doping for the given device structure.

The source doping concentration was set to 2e19 cm^{-3} for the task of optimizing the GeSn/SiGeSn system. The Si content in SiGeSn (x) and the Sn content in GeSn (y) were varied over a range of suitable values. The pseudopotential method was used to extract the band structure parameters for the BTBT model for each x and y. The relaxed valence band offset was determined by using the expression given in Ref. [18] using Jaros' analytical model [19]. The simulated device characteristics are plotted in the form of contour diagrams in Figs. 5 and 6. As the gate voltage is increased, the tunneling path starts at the p++/n junction. Since the pn-junction coincides with the heterojunction of the device, the onset of tunneling and the subthreshold slope are influenced by the Γ-valley CB offset at the GeSn/SiGeSn hetero-interface. Therefore, the shape of the contours of SS (Fig. 5(a)) resembles that of the contours of the Γ-valley CB offset (Fig. 5(b)) for smaller values of x. This is a result of suppressed inter-material tunneling ("point tunneling") with increasing CB offset. Since point tunneling

TABLE II: EPM parameter values for Si and Ge

Parameter	Unit	$Si_{0.5}Ge_{0.5}$		Si	
		Direct	Indirect	Direct	Indirect
E_g	eV	–	0.984	–	1.106
$m_C\langle 100\rangle$	m_0	0.103	0.194	0.405	0.198
$m_{LH}\langle 100\rangle$	m_0	0.125	0.125	0.189	0.189
Degeneracy	1	2	8	2	8
gD^2_{op}/ρ	J^2mkg^{-1}	–	3.54e-21	–	3.54e-21
Δ_C	eV	1.355	0.0	2.251	0.0
ϵ_{op}	meV	–	13.8	–	19.0

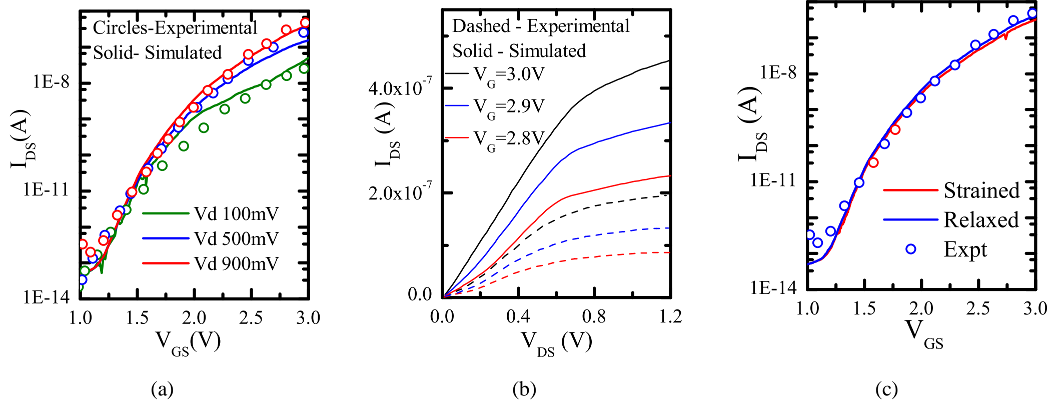

Fig. 3: Results of 3D simulation of the TFET shown in Fig. 2. (a) Comparison of simulated and experimental I_{DS}-V_{GS} characteristics, and (b) I_{DS}-V_{DS} characteristics of the device. The parameters for fully relaxed SiGe layer on Si are used in the simulations (listed in Table II). (c) Comparison of simulated I_{DS}-V_{GS} characteristics by assuming either strained and relaxed SiGe layer.

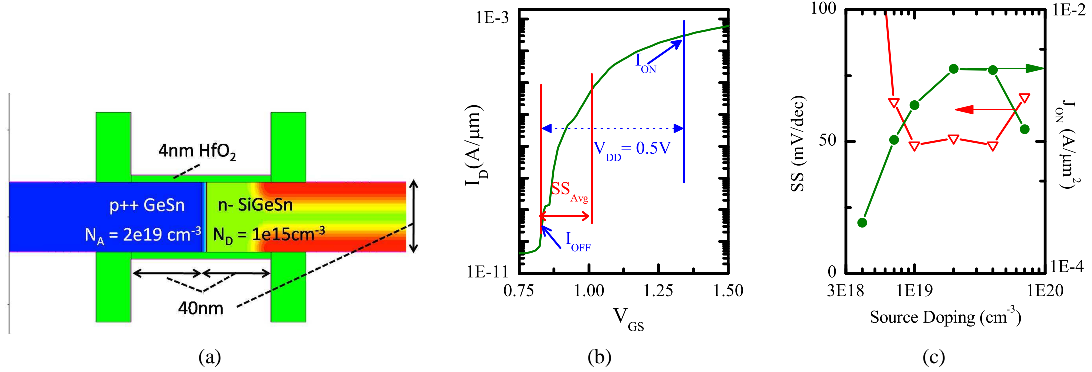

Fig. 4: (a) Structure of the double-gate TFET used in 2D simulations. (b) Definitions of average SS and on-state current in this work. SS is averaged over four decades of I_{DS} starting from I_{OFF}. I_{ON} is the output current at V_{OFF}+0.5 V. (c) Variation of SS and on-current with doping concentration. Degradation of both quantities at high doping levels is a result of quantization in the channel.

occurs on larger tunnel paths due to low doping level in SiGeSn, it degrades the SS. Therefore, suppression of point tunneling improves the SS of the TFET. For larger values of the offset, this effect saturates and the SS is determined by the size of the off-state leakage current caused by SRH generation. Since most of the depletion region is located in SiGeSn, the rate of SRH generation is mainly determined by the band gap of SiGeSn. Therefore, at high x the shape of the contours of SS resembles that of the SiGeSn band gap. The apparent anomaly in the contour shape of SS at the bottom right corner is a result of the increased direct gap of GeSn with decreasing Sn content. From the above three observations it may be concluded that Γ-valley CB offset, SiGeSn band gap, and GeSn direct band gap influence the SS of the heterojunction device. In Fig. 6, SS and on-state current density are plotted as function of the composition of the GeSn/SiGeSn alloy system. Figs. 6(b) and 6(c) provide the contour diagrams of the SS and the on-state current density, respectively, for any given x and y, while Fig. 6(a) gives the Sn content in SiGeSn for given x (Si content in SiGeSn) and y (Sn content in GeSn) thus covering the full composition range of the alloy system. It has been observed that the growth of SiGeSn with both high Si and high Sn content might not be possible. The GeSn active layer might also introduce additional constraints on the composition of the SiGeSn layer. Thus, Fig. 6 would allow technologists to choose the right alloy composition taking into account the constraints of the fabrication process as well as the desired device performance.

IV. Conclusion

A study of the GeSn/SiGeSn heterostructure system for heterojunction TFET applications has been performed in this work. The pseudopotential parameters for Sn were obtained by fitting calculated band energies to experimental data. The band structure parameters required to model BTBT in device simulations were obtained by pseudopotential calculations. The results of 3D simulations of $Si_{0.5}Ge_{0.5}$/Si heterostructure

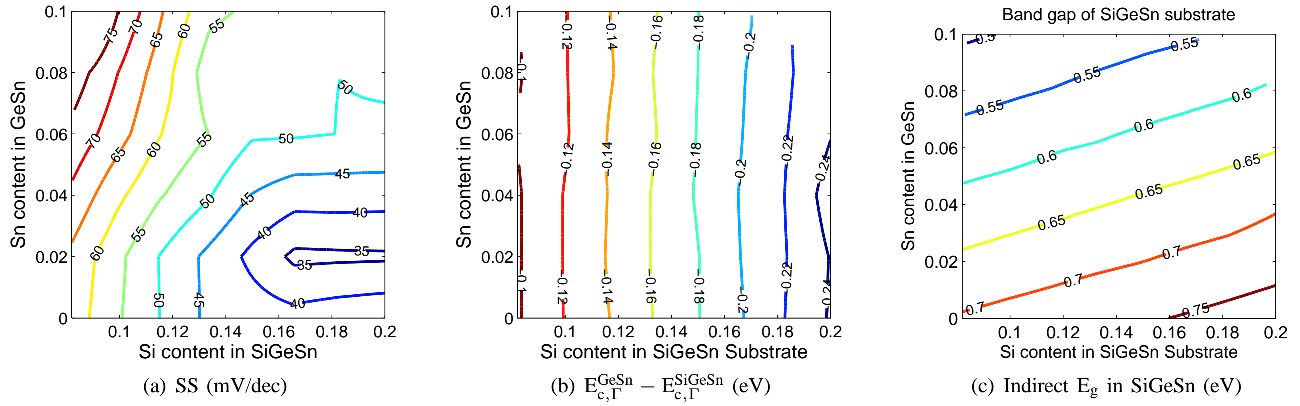

(a) SS (mV/dec) (b) $E_{c,\Gamma}^{GeSn} - E_{c,\Gamma}^{SiGeSn}$ (eV) (c) Indirect E_g in SiGeSn (eV)

Fig. 5: Contour diagrams showing the effect of the Γ-valley conduction band offset and the band gap in SiGeSn on the SS. The Si content in SiGeSn and the Sn content in GeSn are plotted on the x- and y- axes, respectively. Only the alloy compositions with *zero* strain are considered. Due to this constraint, the Sn content in SiGeSn becomes fixed as soon as the two aforementioned mole fractions are fixed.

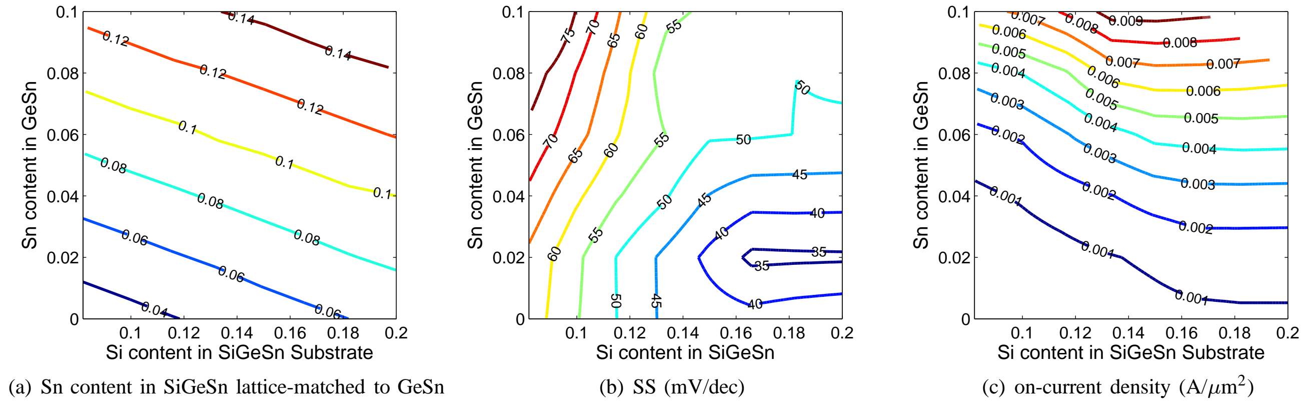

(a) Sn content in SiGeSn lattice-matched to GeSn (b) SS (mV/dec) (c) on-current density ($A/\mu m^2$)

Fig. 6: The contour diagrams (a), (b), and (c) relate the compositions of the GeSn/SiGeSn alloy system to SS and on-current density obtained by simulating the device structure in Fig. 4(a). These contours can be used to extract an approximate alloy composition to achieve given SS and J_{ON} values. For example, the diagrams show that the $GeSn_{0.2}/Si_{0.14}GeSn_{0.06}$ alloy system can provide a slope of 40mV/dec and an on-current density of $1 mA/\mu m^2$.

TFETs were found to be in reasonable agreement with the measurements, asserting the efficacy of the BTBT parameters obtained by the EPM. The device simulations of a double-gate GeSn/SiGeSn TFET have shown that a doping of $2e19\,cm^{-3}$ provides maximum on-current as well as a steep subthreshold slope. The results over a broad range of alloy compositions suggest that the Γ-valley conduction band offset at the GeSn/SiGeSn interface, the band gap of SiGeSn, and the direct band gap of GeSn all affect the subthreshold swing. The on-state current density is primarily determined by the direct band gap in GeSn.

References

[1] S. Gupta et al., J. Appl. Phys. **113**, 073707 (2013).

[2] R. Kotlyar et al., Appl. Phys. Lett. **102**, 113106 (2013).

[3] S. Wirths, et al., Appl. Phys. Lett. **102**, 192103 (2013).

[4] Synopsys Inc., Sentaurus Device Monte Carlo User Guide, Version 2013.03, Mountain View, California, (2013).

[5] S. Sant et al., J. Appl. Phys. **113**, 033708 (2013).

[6] P. Aelle et al., Appl. Phys. Lett. **84**, 888 (2004).

[7] G. Grzybowski et al., Appl. Phys. Lett. **101**, 072105 (2012).

[8] R. Chen et al., Appl. Phys. Lett. **99**, 181125 (2011).

[9] J. Mathews et al., Appl. Phys. Lett. **97**, 221912 (2010).

[10] G. He et al., Phys. Rev. Lett. **79**, 1937 (1997).

[11] A. Tonkikh et al., Appl. Phys. Lett. **103**, 032106 (2013).

[12] V. D'Costa et al., Phys. Rev. Lett. **102**(10), 107403 (2009).

[13] Synopsys Inc., Sentaurus Device User Guide, Version 2013.03, Mountain View, California, (2013).

[14] S. Richter et al., IEEE ULIS'13, p.25 (2013).

[15] E. O. Kane, J. Phys. Chem. Solids **12**, 181 (1959).

[16] E. O. Kane, J. Appl. Phys. **32**, 83 (1961).

[17] O. Penzin et al., IEEE Trans. on Elec. Dev. 58, p. 1614 (2011).

[18] P. Moontragoon et al., J. Appl. Phys. **112**, 073106 (2012).

[19] M. Jaros, Phys. Rev. B **37**, 7112 (1988).